

A Large-Area Search for Low Mass Objects in Upper Scorpius I: The Photometric Campaign and New Brown Dwarfs

Catherine L. Slesnick, John M. Carpenter, & Lynne A. Hillenbrand

Dept. of Astronomy, MC105-24, California Institute of Technology, Pasadena, CA 91125

cls@astro.caltech.edu, jmc@astro.caltech.edu, lah@astro.caltech.edu

ABSTRACT

We present a wide-field photometric survey covering ~ 200 deg² toward the Upper Scorpius OB association. Data taken in the R and I bands with the Quest-2 camera on the Palomar 48-inch telescope were combined with the 2MASS JHK_S survey and used to select candidate pre-main sequence stars. Follow-up spectroscopy with the Palomar 200-inch telescope of 62 candidate late-type members identified 43 stars that have surface gravity signatures consistent with association membership. From the optical/near-infrared photometry and derived spectral types we construct an HR diagram for the new members and find 30 likely new brown dwarfs, nearly doubling the known substellar population of the Upper Scorpius OB association. Continuation of our spectroscopic campaign should reveal hundreds on new stellar and substellar members.

Subject headings:

1. Introduction

The Upper Scorpius OB Association (USco) is the closest (145 pc; de Zeeuw et al. 1999) young OB association to the Sun with 114 known high mass Hipparcos stars. At an age of ~ 5 Myr (Preibisch et al. 2002), this cluster is at an intermediate age between very young star forming regions and older open clusters where samples are sparser and studies of processes such as circumstellar disk dissipation are critical. Recent mid-infrared work by Mamajek et al. (2004) and Silverstone et al. (2006) indicates that by ~ 10 Myr dust is removed from the inner few AU of circumstellar disks for $\gtrsim 85\%$ of stars, whereas $\sim 80\%$ of young 1 Myr stars in Taurus still retain their disks at these radii (Kenyon & Hartmann 1995; Skrutskie et al. 1990). This evolution in circumstellar material corresponds to the stage when planets are thought to be forming. Meteoritic evidence suggests the timescale for dissipation of our

own solar system’s nebula was on order of $\sim 10^7$ yr (Podosek & Cassen 1994). Further, discovery of ^{60}Fe in meteorites argues that short-lived radionuclides were injected into the solar system’s early protoplanetary disk from the explosion of a nearby supernovae (Desch & Ouellette 2005; Tachibana & Huss 2003). The evidence strongly suggests that our solar sytem was formed in an OB association similar to USco. Therefore, if we are to understand our own earth’s origins, we must study the evolution of OB association members during planet-building stages.

A major difficulty faced by studies of the USco region is that the Hipparcos members alone span >130 deg² on the sky. Obtaining a complete census of the association’s low mass population is thus a formidable task as one must identify faint objects over a very large spatial region. While there exist several techniques to identify young stars not associated with molecular gas, many of them are also accretion diagnostics. For example, a common method is to search for strong H α emission (Ardila et al. 2000) produced in outflow or accretion flows (see Section 3.4), or near-infrared excess emission associated with warm inner accretion disks. While accretion can terminate over a wide range in age (1–10 Myr), the median lifetime of optically thick accretion disks is closer to 2–3 Myr (Haisch et al. 2001; Hillenbrand 2006). Therefore, surveys to look for accretion signatures alone will not garner a full census of a 5 Myr association.

Enhanced chromospheric and coronal activity can last well beyond accretion timescales. This activity is linked with X-ray emission (Ku & Chanan 1979; Feigelson & DeCampli 1981) though the exact cause of this phenomenon is still not fully understood (Preibisch et al. 2005). Many previous large-scale efforts in USco have successfully utilized Einstein data (Walter et al. 1994) or the ROSAT All Sky Survey (RASS; Preibisch et al. 1998,1999) to identify hundreds of low and intermediate mass association members. However, neither the Einstein observations nor the RASS were sensitive enough to detect faint X-ray emission from the lowest mass stars and brown dwarfs.

Recently, deep, multicolor imaging surveys combined with spectroscopic follow-up have proved successful in identifying both the youngest classical T Tauri-type objects and more evolved very low mass stars and brown dwarfs in a variety of young regions. Young PMS objects still undergoing contraction towards the main sequence are redder and more luminous than their main sequence counterparts. Spectroscopic follow-up observations allow assessment of surface gravity diagnostics which can be used to distinguish young PMS stars from reddened field dwarfs and background giants. Previous imaging and spectroscopic surveys in USco include work by Preibisch et al. (2001,2002) who selected candidate association members based on optical magnitudes and colors obtained from photographic plates in the United Kingdom Schmidt Telescope survey fields. Their spectroscopic survey of 700 candi-

dates over 9 deg^2 using the 2dF multifiber spectrograph yielded 166 new PMS stars based on the presence of lithium in their spectra. Martín et al. (2004) selected candidate young objects from the DENIS I, J survey and obtained spectra of 36 targets. Of these 28 were confirmed to be new low mass association members based on surface gravity diagnostics. Ardila et al. (2000) used R, I, Z photographic photometry to identify candidate members within an $80' \times 80'$ area of the association. Spectroscopic data were obtained for 22 candidates, 20 of which were determined to exhibit $H\alpha$ emission indicating possible membership. Thus far, over 300 low mass ($M < 0.6 M_{\odot}$) members have been identified in USco through X-rays, $H\alpha$ emission, photometry and/or spectroscopy. However most searches have been limited to small subregions or bright objects. Given the USco upper IMF, and assuming the high and low mass objects share the same spatial distribution, Preibisch et al. (2002) estimate the entire USco region should contain >1500 young, low mass objects with $M < 0.6 M_{\odot}$, most of which are yet to be discovered.

Building on previous work in this region, we have completed a large-area optical photometric survey of $\approx 200 \text{ deg}^2$ in and near USco. We combine these data (section 2) with 2MASS J, H, K_S photometry to select candidate young PMS objects. In section 3 we present newly-obtained optical spectra for 62 candidate young brown dwarfs and low mass stars. These spectra allow us to determine spectral type and confirm membership for photometrically-selected candidates. Finally in section 4, we derive an HR-diagram and discuss noteworthy new members.

2. Observations

2.1. Photometric Monitoring and Data Processing

Photometric observations were taken with the Quest-2 Camera (Rabinowitz et al. 2003) on the 48-inch Samuel Oschin Schmidt Telescope at Palomar Observatory. The Quest-2 Camera is a large-area mosaic of 112 CCDs arranged in a grid of 4 columns by 28 rows. Each CCD has 600×2400 pixels with a scale of $\sim 0.8''/\text{pixel}$. The camera covers a $3.6^\circ \times 4.6^\circ$ field of view. Taking into account gaps between columns and chips the total sky coverage is 9.4 deg^2 per pointing. Each of the four columns views the sky through a separate filter.

Data were obtained in driftscan format using U, B, R, I filters. Any given patch of sky is observed over the entire 2400-pixel width of four separate CCDs (1 per filter) in one of the 28 rows. Charge is continuously read out of each CCD throughout the observation and the final data product is a strip of uniform width in declination and time-dependent length in right ascension. Three scans, centered at $\delta = -15.7^\circ, -19.5^\circ, -23.3^\circ$, were each observed between

RA of 15h46m and 16h36m. The scan centered at $\delta = -19.5^\circ$ was observed 3–4 times per night on seven consecutive, photometric nights between 20–26 June 2004. The other two scans were observed once during this period. Spatial coverage is shown in Figure 1. Because several CCDs have failed since installation due to bad connections or faulty chips, our spatial coverage within the survey region is not uniform. Five of 28 CCDs in the I column, five in the R column and four in the B column are not fully functional. The CCDs are less sensitive in the U -band than anticipated and very few source detections were obtained. As discussed in Section 2.3, we are primarily concerned with selecting faint red objects as candidate young low mass stars, the majority of which do not have a B -band detection. We therefore exclude the U and B data from the remainder of this discussion.

When operated in driftscan format, the Quest-2 camera generates ≈ 50 GB of raw, compressed data in a single night. To efficiently process such a large volume of data, the Quest-2 Collaboration (Rabinowitz et al. 2003) has developed automated data reduction software (Andrews 2003). Each of the CCDs is treated as a separate instrument during reductions and therefore we explain the procedure for a single chip. The software first performs the basic bias subtraction and flat-fielding. The bias level for a given column of the CCD is computed by median-combining 25 rows in the overscan region and subtracted. Dark subtraction and flat-fielding cannot be carried out using the standard techniques of pointed observations. Instead, skyflat and dark driftscans were taken on the first night of observations. Each calibration image was first divided into 240 600x10 pixel segments and then median-combined using the IRAF IMSUM task to remove cosmic rays (darks) or stars (skyflats). The resulting 600x10 pixel image was then averaged into a single row of 600 pixels using the IRAF BLKAVG task. The averaged dark and flat rows were subtracted and divided respectively from each row of data.

After pre-processing, the pipeline generates a point-spread function (PSF) for every frame (600x2000-pixels) of data which it uses to detect sources. It registers detections from all four filters and generates an astrometric solution from the USNO-A2 catalog. We have matched detections within a $0.8''$ radius from up to 24 different scans in the monitoring region. For each source we computed new coordinates by averaging together coordinates from individual scans and find typical astrometric residuals for individual detections about the mean to be $\pm 0.1''$.

The Yale pipeline generates photometry both from a range of apertures and from PSF function fitting. We compared PSF and aperture photometry and found the aperture photometry produced more consistent results for sources observed in multiple scans (see Section 2.2 for a detailed discussion of photometric reliability). We therefore chose to rely on aperture photometry despite the potential advantages of PSF fitting for crowded stars. The

pipeline measures all objects through an aperture of half-width 3.5 pixels (found to produce the highest signal to noise photometry for a subset of bright, isolated stars). To account for zeropoint variations between chips we applied the calibrations derived by the Quest-2 instrument group at Yale (Jerke et al. private communication). These calibrations also converted Quest-2 instrumental magnitudes into the Johnson photometric system.

We accounted for small atmospheric transparency changes during the night and between nights by applying a photometric offset to every scan as a function of RA. We selected a subset of calibrator stars from our source catalog that were detected in at least 20 out of 24 of the $\delta = -19.5$ monitoring scans, and had no neighbors within $5''$. For each star and filter an uncertainty-weighted average magnitude of all detections was calculated along with the difference between that average magnitude and the magnitude measured on each individual scan. For every chip we created a catalog of offsets by stepping through in RA every 25 calibrator stars and calculating a median offset value. We applied these offsets of up to 0.25 mag to the entire data set as a function of RA and CCD chip by linearly interpolating in RA values. For the high ($\delta = -15.7^\circ$) and low ($\delta = -23.3^\circ$) declination scans which overlap only the top and bottom 0.8 deg of the monitoring scan region, we calculated a scan offset as a function of RA using the same procedure outlined above but averaging together all columns of overlap with the mid-declination scans, rather than chip by chip. We find this procedure produced magnitudes consistent with those derived from the multiple-scan region at the 7% (R) & 2% (I) levels for objects in the overlap region. Finally, to account for differences in airmass between the Yale calibrator scans and USco scans we applied offsets of 0.08 & 0.05 mag for the R, I data (Parrao & Schuster 2003) as derived at San Pedro Mártir and consistent with typical Palomar extinction coefficients.

2.2. Precision and Accuracy

In this section we use photometry from the monitoring scans to assess the relative precision of the photometric data. We find photometric precision to be CCD dependent and give values for best, worst and typical scenarios. The photometric accuracy is harder to quantify at this time. Zeropoints for individual CCDs and conversions from Quest-2 to Johnson photometry have not yet been finalized by the Quest-2/Yale instrument team. To place some constraints on data accuracy we have matched the R - and I -band photometry to photometry from Ardila et al. (2000) and examine consistency.

For each source in the multiple scan region, an uncertainty-weighted average and the RMS deviation of the individual measurements was calculated. The 112 CCDs are of varying quality which leads to non-uniform photometric characteristics. Figure 2 shows the RMS as

a function of magnitude for a single CCD for sources detected at least ten times. The top panel shows data for the CCD in row 13, column 1 (R filter), one of the most reliable CCDs. The bottom panel shows data for an adjacent CCD in row 14, column 1, representative of a typical CCD. The best CCDs have RMS values from ~ 0.01 mag for the bright stars and increasing to ~ 0.05 mag by $R=19$ and $I=18.5$. A typical CCD has RMS ~ 0.03 mag at the bright end to ~ 0.08 mag at the faint end. We find six CCDs to be of poor quality with RMS ranging from ~ 0.07 – 0.15 mag at the bright and faint ends.

The accuracy of the photometric transformations from the Quest-2 to the Johnson system is harder to quantify since differences both in zeropoints between chips and in conversion between photometric systems must be accounted for. The Quest-2 instrument team at Yale has matched Quest-2 observations in the north to Sloan Digital Sky Survey (SDSS) photometry and derived conversions for each chip from Quest-2 to SDSS (converted to the Johnson system; Fukugita et al. 1996). We have used the current calibrations and attempted to quantify the accuracy of the photometry presented here by comparing our data to that of Ardila et al. (2000) who observed ~ 14 deg² in USco in the Cousins R and I bands. Figure 3 shows the difference between Quest-2 Johnson $R - I$ colors and those from Ardila et al. (2000) converted from the Cousins to the Johnson system (Ferne et al. 1983) as a function of Quest-2 Johnson R magnitude. Error bars of ± 0.18 mag reflect average root-sum squared uncertainties from both data sets: $\langle \sigma_{R-I} \rangle = 0.14$ in the Ardila et al. (2000) photometry (private communication) and $\langle \sigma_{R-I} \rangle = 0.11$ for the Quest-2 photometry assuming typical magnitude uncertainties of 0.08 mag for faint stars. The average difference between the two data sets is 0.01 mag with an RMS deviation of 0.17, consistent with uncertainties.

From histograms of all detections for the R and I filters, we find a turnover in number of objects detected at $R \sim 19$ mag and $I \sim 18$ mag with a substantial number of detections out to $R \sim 20$ and $I \sim 19$. We believe the precision of our photometry to be $\lesssim 0.08$ mag for $\sim 90\%$ of stars brighter than these values. Both R and I data saturate for stars brighter than ~ 13 mag.

2.3. Candidate Member Selection

The detection algorithm in the Yale data pipeline was written to find very faint quasars and therefore uses a low detection threshold. To produce a reliable catalog of sources, we first required an object to be detected in both the R and I filters. Further, we matched our entire dataset to the 2MASS All Sky Catalog (Cutri et al. 2003) and considered stars as potential candidates only if they had a 2MASS counterpart within $2''$. This cut biases our final catalog against faint blue objects to which 2MASS is not sensitive. Of the ~ 1.5 million

objects in our source catalog, $\sim 500,000$ have 2MASS counterparts. However, because we are interested only in objects redder than a 30 Myr isochrone in an optical color-magnitude diagram (see below for details), and bright enough to be observed spectroscopically ($R \lesssim 20$ mag), this bias does not affect candidate selection in practice. Figure 4 shows contour optical color-magnitude diagrams of all Quest-2 sources (black) and those with 2MASS detections (red). As can be seen, the red side of the color-magnitude diagram brighter than $R \sim 20$ is not substantially affected by excluding objects without a 2MASS detection.

The final photometric catalog that we use to select candidate association members contains $\sim 500,000$ sources with R, I, J, H , & K_S detections, most of which are field stars. However, buried in these $\sim 500,000$ sources are several thousand bona fide low mass members of USco. We use this data-set to select candidate PMS stars based on an optical color-magnitude diagram indicating they could be young USco members. In Figures 5–7 we present color-magnitude and color-color diagrams used in PMS candidate selection. For the work presented here, we used three levels of selection criteria. In each Figure objects which meet the outlined selection criteria *and* all previous selection criteria are shown as discreet points. In Figure 5 we show the $R, R - I$ color-magnitude diagram for all sources matched to 2MASS. About 60,000 sources with $R < 5 \times (R - I) + 11$ appear younger than ~ 30 Myr based on theoretical isochrones (D’Antona & Mazzitelli 1997 & 1998¹, hereafter DM97) and could be PMS objects.

2MASS photometry was used to further refine the candidate sample. In Figure 6 we show a near-infrared color-color diagram. Solid lines represent the dwarf (bottom line) and giant (top line) loci. The dashed line represents the classical T Tauri star locus as defined by Meyer et al. (1997). Beyond this point we considered only objects which had ‘good’ 2MASS photometry (quality flag ‘A’) in all three J, H, K_S bands. Any star with $J - H, H - K_S$ colors consistent with those expected for background giants ($(J - H) > 0.6 \times (H - K_S) + 0.6$) was excluded.

After applying the above selection criteria we identified $\sim 20,000$ candidate new young USco members over ~ 200 deg². Due to interstellar extinction and distance effects, optical and near-infrared colors and magnitudes alone are not a unique indicator of youth; therefore, it is necessary to obtain spectroscopic follow-up observations to determine an object’s spectral type and confirm low surface gravity consistent with that of young association members. We began a spectroscopic follow-up program with 5 observing nights in June 2005 using the Double Spectrograph on the Palomar 200-inch Telescope and 5 more in July 2005 using Hydra on the CTIO 4-m Telescope. With the Palomar spectroscopic observations discussed

¹The 1998 models are a web-only correction at $< 0.2 M_\odot$ to their original 1997 work.

here, we chose to target potential new brown dwarfs and very low mass stars to take full advantage of the high sensitivity of the Double Spectrograph. We therefore selected only the reddest candidates satisfying $R < 2.57 \times (R - K_S) + 13$ in an $R, R - K_S$ color magnitude diagram (Figure 7) and focused primarily on the faintest ($R > 18.5$) targets. With hydra/CTIO we took spectra of close to 1000 brighter ($15 < R < 18.5$) candidates, leading to new higher mass (spectral type G-M) USco members which will be discussed in a forthcoming paper. After applying this last selection criterion we were left with ~ 1000 candidates suitable for spectroscopic follow-up with the Double Spectrograph, ~ 200 of which are fainter than $R=18.5$.

2.4. Optical Spectroscopy

Moderate resolution spectra of 65 objects (Table 1; shown as large circles in Figures 5–7) were obtained during the nights of 2005 June 8–12 using the Double Spectrograph on the 200-inch Palomar telescope. Of these, 41 were fainter than $R \sim 18.5$ corresponding to $\sim 20\%$ of the faint candidates meeting all of the selection criteria detailed in Section 2.3. Because Quest-2 is a new instrument and software is continuously being updated, the photometric data has been re-reduced several times. Photometry for three of the spectral targets has changed significantly since the spectroscopic observations were taken such that they would no longer be considered candidates. As expected, all three were determined to be field dwarfs based on their spectra. For completeness these three sources are shown in the figures and listed in Table 1, but otherwise are not discussed further.

Data were taken using the red side of the Double Spectrograph which has a 1024×1024 CCD with $24\text{-}\mu\text{m}$ pixels. We used a $2.0''$ entrance slit, 5500 \AA dichroic and 316 lines/mm grating blazed at 7500 \AA which gave a wavelength coverage of $6300\text{--}8825\text{ \AA}$ at resolution $R \sim 1250$. Typical exposure times were 600–900 seconds and we were able to observe objects as faint as $R \sim 20$ in 1800 seconds with $\text{SNR} \sim 30\text{--}40$. Spectrophotometric standard stars (Massey et al. 1988) were observed throughout every night for flux calibration. All sources, including standards, were pre-processed, extracted and flux-calibrated using standard IRAF tasks.

3. Spectral Analysis

The $\lambda 6300\text{--}8825\text{ \AA}$ wavelength regime contains many temperature-sensitive and surface gravity-sensitive features diagnostic for classifying late-type stars. To ensure that we could

accurately classify our program stars, we observed a range of spectral main-sequence standards (K5–L1.5), giant standards (K7–M9), and previously-identified USco objects (K3–M8; Preibisch & Zinnecker 1999, Ardila et al. 2000, Martín et al. 2004). In addition, we took observations of spectroscopically confirmed 1-Myr Taurus members and 100-Myr Pleiades stars during an observing run in December 2004 with the same telescope and instrument set-up. Together these observations provide a large range in both temperature and surface gravity which we use for aid in classifying program stars.

In this section we use molecular absorption features to derive a spectral type for each object. From atomic and molecular surface gravity diagnostics we determine which objects have low, PMS-type gravity and are therefore likely association members. The effects of reddening and veiling are explored and considered in both temperature and gravity determination.

3.1. Temperature Classification

Figure 8 shows spectra for dwarf stars of spectral types M3, M6 & M8. The dominant molecular absorption features present are attributed to titanium-oxide (TiO), the strongest of which are labeled. TiO absorption increases from mid-K thru \sim M7 spectral types at which point its strength begins to decrease and vanadium oxide (VO) absorption starts to dominate spectra by early L types. We have defined or adopted from the literature several band indices to measure the strength of the TiO absorption features. We find two in particular to be diagnostic. TiO-7140 measures the strength of TiO λ 7140 Å absorption compared to a continuum band at λ 7035 Å (Willing et al. 2005). This index is defined as $\text{TiO-7140} = F_{\lambda 7035} / F_{\lambda 7140}$ with bandwidths of 50 Å. TiO-8465 is a new index defined by us ($\text{TiO-8465} = F_{\lambda 8415} / F_{\lambda 8465}$) to measure the strength of TiO λ 8465 Å absorption compared to a continuum band at λ 8415 Å. Bandwidths for the TiO-8465 index are 20 Å. In Figure 8, light and dark shaded regions respectively show location of the TiO and continuum bands used in our analysis.

The left panel of Figure 9 shows a plot of TiO-8465 vs. TiO-7140; black spectral types are measured indices for field dwarf spectra and blue spectral types are measured indices for known USco and Taurus members. This diagram is particularly useful for classifying objects with spectral types \sim M3–L3. We find no surface gravity dependence between measured indices for the dwarf, USco, and Taurus standard objects. In the right panel of Figure 9, green circles correspond to measured indices for program stars. As can be seen, the program star measurements follow the locus laid out by the standard stars extremely well. We find six outliers which sit below the main locus of data points. In all six cases, the star is confirmed

to exhibit low gravity signatures (Section 3.2) and we attribute the position in Figure 9 to a small amount of veiling present in its spectra (Section 3.3). These objects are further discussed in Section 4.2.

Spectral types were determined first from quantitative analysis using an object’s measured TiO indices. More weight was given to the value of the TiO-8465 index which we find particularly insensitive to the effects of reddening and veiling, as discussed in Section 3.3. Using the TiO indices alone we can not uniquely recover spectral types for the dwarf and PMS standards. This ambiguity is due in part to uncertainties in published spectral types and in part to systematic differences between spectral classification schemes of different authors. Therefore, it was necessary to examine each spectrum by eye and use the information from the entire spectral range in final type determination. All program spectra were compared visually to a large grid of standard spectra. Typical revisions to the quantitative spectral types were at the level of 1–2 subclasses.

3.2. Surface Gravity Assessment

Accurate spectral classification requires determining both the type (indicative of temperature) and the luminosity class (indicative of gravity) of our candidates. Several robust surface gravity sensitive features exist in the $\lambda 6300\text{--}8800\text{ \AA}$ spectral regime which can be assessed in low resolution spectra and used to distinguish high gravity dwarf stars from younger PMS objects still undergoing contraction. The three most prominent features are due to NaI ($\lambda 8183$ & $\lambda 8195\text{ \AA}$) and KI ($\lambda 7665$ & $\lambda 7699\text{ \AA}$) lines and CaH molecular absorption at $\lambda \lambda 6975\text{ \AA}$. Figure 10 shows a sequence of three M6 standard stars: a high-gravity main-sequence star (GJ406), a 5-Myr intermediate-gravity USco object (DENIS-P16007.5-181056.4) and a 1-Myr lower-gravity Taurus object (MH05). Gravity sensitive absorption features are labeled and increase in strength with increasing stellar age and gravity.

We have developed a gravity-sensitive index, Na-8189, which measures the strength of the Na I doublet at $\lambda 8189\text{ \AA}$ compared to the strength of a continuum band at $\lambda 8150\text{ \AA}$. Each band is 30 \AA wide. The index is defined as $\text{Na-8189} = F_{\lambda 8189}/F_{\lambda 8150}$. The left panel of Figure 11 shows a plot of the temperature-sensitive TiO-7140 index vs the gravity-sensitive Na-8189 index. Black and blue spectral types respectively represent measured indices for dwarfs and known PMS stars, similar to Figure 9. Cyan spectral types show measured indices for low-gravity giant standards. We find the Na-8189 index to be a robust diagnostic that clearly separates low, intermediate and high gravity for spectral types later than M2. Objects with spectral types earlier than $\sim M2$ do not exhibit substantial Na I absorption. Measured Na-8189 indices for 100-Myr Pleiades stars are indistinguishable from those for

dwarfs at similar spectral types. In the right panel of Figure 11 green circles correspond to measured indices for program stars. A large fraction, 43/62, of the candidate objects have measured Na-8189 indices consistent with their having surface gravity less than that of field dwarfs at similar spectral types.

Gravity signatures in all spectra were verified visually. For only one star did we find a visual assessment which disagreed with the quantitative result of the Na-8189 index. SCH16224384-19510575 appears to be a giant star based on the Na-8189 index alone but was determined from visual inspection to be a young, PMS-type object based on the overall shape of its spectrum longward of $\sim 8200\text{\AA}$ and strong $H\alpha$ emission (Section 3.4). This object is discussed further in Section 4.2.

3.3. Stellar and Interstellar Processes Which Can Affect Spectral Classification

In this section we explore possible biases in the spectral classification due to the effects of stellar and interstellar reddening, or spectral veiling produced either from a cool circumstellar disk or from a hot accretion shock. We assess the effects these processes can have both on the quantitative TiO and Na indices and on the overall appearance of a spectrum.

3.3.1. Extinction

Hot OB stars have dispersed much of the dense gas and dust in the USco region; therefore, we do not expect individual members to show more than moderate extinction. We derived an approximate A_V measurement for each star by visually dereddening its spectrum until its slope matched that of a standard star of the same spectral type. We find that 80% of the newly identified members have $A_V < 1$ based on spectral slope from $\lambda 6300\text{--}8825\text{ \AA}$, and only three appear to have A_V between 2 and 3 mag. More precise extinction values are derived from each object’s spectral type and colors in Section 4.1, and in all cases we find agreement to within one magnitude of our visual estimate.

To assess the effect reddening has on our quantitative classification indices we artificially reddened all standard stars by $A_V=10$ mag, the maximum extinction inferred from large-beam dust measurements towards our survey region excluding the young ρ Ophiuchus molecular cloud core (Schlegel, Finkbeiner, & Davis 1998). We measured index strengths for artificially reddened spectra and find average index shifts of -0.1 for TiO-7140 and -0.04 for TiO-8465. As can be seen from Figure 9, index shifts at this level are not sufficient

to affect our quantitative temperature determination from TiO indices at the 0.5 subclass level. Ten magnitudes of extinction could affect the Na-8189 index by an average shift of -0.05. However at a level of reddening more consistent with actual measured values for new members ($A_V \lesssim 2$; Section 4.1, Table 2), we find a much more moderate shift of -0.01 which would not be sufficient to make a dwarf star look like a PMS star for objects between M2 and M9.

3.3.2. Optical and Near-infrared Veiling

A young star spectrum can be veiled at UV/optical wavelengths due to excess emission from an accretion shock, and in the infrared due to thermal emission from dust grains in a circumstellar disk. In both cases the excess emission veils (decreases) the strength of the molecular absorption features used in classification and will cause a star to be systematically classified too hot (early) in spectral type. The veiling index is defined as $r_\lambda = F_{\lambda ex}/F_{\lambda ph}$, where “ex” indicates excess and “ph” indicates photosphere. We tested several scenarios to determine the existence and magnitude of any bias in the spectral types attributable to veiling.

First, we added to all spectra a $T_{eff}=1400$ K blackbody consistent with a cool disk around a low mass star or brown dwarf at a veiling level of $r_K=0.6$, corresponding to the median near-infrared veiling value for K7-M0 classical T Tauri stars (Meyer et al. 1997). The Wein tail of such a blackbody could affect our spectral indices around $0.8\mu m$. We remeasured indices for veiled standard spectra and found, as expected, excess thermal emission from a cool disk has very little effect on optical spectra. Results from veiling experiments are shown for a single star (DENIS-P16007.5-181056.4, M6 USco member; Martín et al. 2004) as connected red symbols in the left panels of Figure 9 and Figure 11. We see similar results for all M-type (SpType > M2) standards artificially veiled using these techniques. The re-derived indices for DENIS-P16007.5-181056.4 plus near-infrared veiling described above are shown as red squares which lie practically on top of the original ‘M6’ blue points in both figures.

Next, we investigated the effects of veiling from a hot accretion shock. We used a value of $r_{6500}=0.6$, equivalent to the average optical veiling value for late K and early M stars (White & Hillenbrand 2004). We added a $T_{eff}=8000$ K blackbody at this level to all standard spectra and re-derived the spectral classification indices (triangle symbols Figures 9 & 11). We experimented by adding a continuum excess of constant flux ($F_{ex} = C$) at the $r_{6500}=0.6$ level (‘X’ symbol Figures 9 & 11), shown by White & Hillenbrand (2004) to be more consistent with observations than a hot blackbody. In both cases, the strength of the

TiO-7140 index decreases substantially while the change in the TiO-8465 and Na-8189 indices are much smaller. For this reason, we rely primarily on the TiO-8465 index for temperature classification and believe our surface gravity assessment from the Na-8189 index to be robust to effects of veiling.

3.4. Emission Lines

The only prominent emission line observed in any of the spectra is $H\alpha$ which, seen in the spectra of young stars and brown dwarfs, is predominantly created via one of two mechanisms. Weak, narrow $H\alpha$ lines are presumed to originate from active chromospheres whereas strong, broad and/or asymmetric lines can be produced from high-velocity, infalling accretion or strong winds. Barrados y Navascués & Martín (2003) have proposed an empirical, spectral-type- $H\alpha$ equivalent width ($W(H\alpha)$) relation to describe the upper limit of non-accreting stars and brown dwarfs based on the chromospheric saturation limit observed in young open clusters. Figure 12 plots measured $H\alpha$ equivalent widths for all spectra as a function of spectral type, shown with the Barrados y Navascués & Martin (2003) empirical accretor/non- accretor division. Four objects (SCH16222156-22173094: M5, SCH16103876-18292353: M6, SCH16224384-19510575: M8, SCH16235158-23172740: M8; see Table 1) exhibit very strong emission ($W(H\alpha) < -60 \text{ \AA}$) at levels substantially above those measured for the majority of sources in our sample and are possibly still undergoing active accretion. High resolution spectroscopy is needed to assess further the evidence for accretion based on line profiles/shape.

3.5. Summary of Spectral Classification and Analysis

We have determined spectral types and surface gravity estimates for 62 objects towards the USco association. These objects were selected as candidate PMS association members based on their optical and near-infrared colors and magnitudes. In all cases, classification was done first using flux ratios of broad molecular absorption lines or narrow atomic lines to continuum levels. Reddening and veiling were accounted for during the spectral classification and gravity assessment processes. All spectral types and surface gravity estimates were confirmed from visual comparison to standard spectra. Unless otherwise noted in Table 1, spectral type errors are $\pm 0.5 \text{ SpType}$.

Table 1 lists optical and near-infrared 2MASS photometry, measured spectral indices, spectral types and $H\alpha$ equivalent widths. We also list a qualitative surface gravity type:

‘USco’ and ‘dwarf’ labels indicate a star has surface gravity signatures consistent with those measured for known USco members or field dwarfs. A value of ‘int’ corresponds to the object having gravity signatures between those of known USco members and field dwarfs, indicating it is likely a more evolved association member, a member of one of the neighboring Sco-Cen subgroups, or a very young field object. As mentioned previously, we find Na-8189 indices for Pleiades objects to be indistinguishable from those measured for dwarf stars. Therefore the ‘int’ objects are most probably between 5 and ~ 100 Myr. For the remainder of this paper we consider all objects with gravity classification ‘USco’ or ‘int’ as new association members.

4. USco Population Analysis

4.1. HR-Diagram

In this section we combine each new member’s spectral type and photometry to derive values for its luminosity and effective temperature and place it on a theoretical HR-diagram. As described in Section 2, the final calibration of Quest-2 optical data is still under revision. Thus, because of the reliability and uniformity of the 2MASS survey we chose to use J -band magnitudes and $(J - H)$ colors to derive luminosities. An empirical fit to BC_J as a function of spectral type was determined from the observational data of Leggett et al. (1996, 2002; spectral types M1-M6.5 and M6-L3). We adopted intrinsic colors, extinction, and effective temperatures using the methods described in Slesnick, Hillenbrand & Carpenter (2004). Derived quantities are given in Table 2.

In Figure 13 we present an HR-diagram for the 43 newly identified low mass members of USco, shown with the PMS model tracks and isochrones of DM97. The most commonly used PMS models for low mass stars and brown dwarfs are those derived by DM97 and Baraffe et al. (1998) which differ primarily in their atmospheric approximations and treatment of convection. No models to date have consistently reproduced dynamical masses for young low mass objects ($M < 1.2 M_\odot$; Hillenbrand & White 2004). We therefore do not attempt to derive masses and ages for new members at this time. Both models suggest similar mass ranges for our data of $0.02 M_\odot < M < 0.2 M_\odot$, though predicted masses for individual objects can vary by up to $0.07 M_\odot$. As illustrated in Figure 13, we have identified a low mass stellar population of age roughly consistent with the 5 Myr age inferred in previous work on the intermediate mass ($6 M_\odot < M < 0.1 M_\odot$) members of USco (Preibisch et al. 2002).

4.2. Interesting Objects

In this section we discuss objects and empirical observations worthy of comment. The one outlier to the main locus of USco points in Figure 13 is object SCH16224384-19510575 which appears over-luminous and extremely young compared to the other sources. This object also has strong $H\alpha$ emission (see Section 3.4) with a slightly asymmetric profile. It is unlikely that this object is a single, extremely young ($<100,000$ yr based on HR diagram placement) association member. The object could be a young, PMS-gravity foreground object that happens to fall within our line of sight. The simplest explanation is that SCH16224384-19510575 is an unresolved binary. Assuming typical seeing at Palomar under photometric conditions of $\sim 1.2''$, any pair with separations $\lesssim 175$ AU would not be resolved in our data. If we assume SCH16224384-19510575 consists of 2 equal-luminosity objects, its placement in the HR-diagram becomes more consistent with the main locus of association members. This effect is illustrated as an arrow plus dotted symbol in Figure 13.

The six objects with measured TiO indices below the main locus of points (see Figure 9) are SCH16103876-18292353 (M6), SCH16202523-23160347 (M5.5), SCH16213591-23550341 (M6), SCH16222156-22173094 (M5), SCH16224384-19510575 (M8), and SCH16235474-24383211 (M6). Three of these objects, one of which is the possible binary discussed above, have very strong $H\alpha$ emission and are possible accretors. Three lie very close (within ~ 1 deg) to the young ρ Oph molecular cloud. However, because ρ Oph and USco lie at approximately the same distance, if they were escaped, $\lesssim 1$ Myr ρ Oph members we would expect to see them exhibit systematically higher luminosities than USco members of similar spectral type. Based on Figure 13, this phenomenon is not observed. All six have a near-infrared excess based on $J - H$, $H - K_S$ colors (Figure 6; Table 1) indicating the presence of an inner circumstellar disk. In every case we find spectral shapes consistent with a small amount of veiling ($r_\lambda \sim 0.1$ – 0.2) in their spectra.

The spatial distribution of the four strong $H\alpha$ emitters (likely accreting objects; boxed on Figure 1) follows a ridge of dust outlined by $100\mu\text{m}$ IRAS emission at the western edge of the association. All four objects are located outside of previous surveys to search for low mass members, and outside most of the known high mass association members (cyan pluses, Figure 1). In general, we find some evidence for a trend of increased luminosity (within a given spectral type) for objects in the western portion of the cloud, independent of declination. Further spectroscopic observations will determine whether there exists a substantial population of young objects in these regions.

5. Summary and Future Work

We have completed a large-area R, I photometric survey in and near the Upper Scorpius region of recent star formation. From these data we selected candidate new PMS association members based on their optical and near-infrared colors and magnitudes. We present here results from the first effort in our spectroscopic follow-up campaign. We observed 62 candidates and determined 43 (70%) to be bona fide new Upper Scorpius members. We derive an HR diagram for new members, mention noteworthy individual objects, and speculate on the spatial distribution of yet undiscovered low mass association members.

At an age of 5 Myr, all objects with spectral type $\geq M6$ are commonly considered to be substellar. Based on this criterion, from the 43 new members we identify 30 new brown dwarfs. Prior to this work, 34 spectroscopically confirmed USco members had been identified at these spectral types (Preibisch et al. 1999, Ardila et al. 2000, Martín et al. 2004). In Figure 14 we present a histogram of the number of brown dwarfs known with the addition of our work (light shading) compared to what was known previously in the literature (dark shading). As can be seen, with this study we have doubled the number of known substellar objects in Upper Scorpius.

In addition to the data presented here, we have taken spectra of ~ 1000 candidates with hydra/CTIO which will be presented in a forthcoming paper. We have IRAC/*Spitzer* data and approved MIPS $24\ \mu\text{m}$ /*Spitzer* observations of 28 of the newly identified brown dwarfs which we analyze in Slesnick, Carpenter, & Hillenbrand (2006).

6. Acknowledgments

The authors would like to thank the entire Quest-2 collaboration and in particular David Rabinowitz, Anne Bauer, Jonathan Jerke and Adam Rengstorf for observing and processing the photometric driftscan data. We are appreciative to Ashish Mahabal and Milan Bogosavljevic for their help in understanding the Quest-2 systematics. We thank Russel White and David Ardila for discussions and insights which helped in our analysis.

REFERENCES

- Andrews, P.A. 2003, PhD thesis
Ardila, D., Martín, E.L., & Basri, G. 2000, *AJ*, 120, 479
Baraffe, I., Chabrier, G., Allard, F., & Hauschildt, P.H., 1998, *A&A*, 337, 403 (BCAH98)

- Barrado y Navascués, D., & Martín, E.L. 2003, *AJ*, 126, 2997
- Buoy, H., Brander, W., Martín, E.L., Delfosse, X., Allard, F., & Bassri, G. 2003, *AJ*, 126, 1526
- Burgasser, A., Kirkpatrick, J.D., Redi, I.N., Brown, M.E., Miskay, C.L., & Gizis, J.E. 2003, *Apj*, 586, 512
- Close, L.W., Siegler, N., Freed, M., & Biller, B. 2003, *ApJ*, 587, 407
- Cutri, R.M., et al. 2003, *Cat* 2246
- D’Antona, F., & Mazzitelli, I. 1997, *Mem. Soc. Astron. Italiana*, 68, 807 (DM97)
- Desch, S., & Ouellette, N. 2005, *PPV*
- Feigelson, E.D., & Decampli, W.M. 1981, *ApJ*, 243, 89
- Fernie, J.D. 1983, *PASP*, 95, 782
- Fukugita, M., Ichikawa, T., Gunn, J.E., Doi, M., Shimasaku, K., & Schneider, D.P. 1996, *AJ*, 111, 1748
- Haisch, K.E., Lada, E.A., & Lada, C.J. 2001, *ApJ*, 553, 153
- Hillenbrand, L.A. 2006, ‘A Decade of Discovery: Planets Around other Stars’, *StScI symposium Series 19*, ed. Livio, in press
- Hillenbrand, L.A., & White, R.J. 2004, *ApJ*, 604, 741
- Kenyon, S.J., & Hartmann, L. 1995, *ApJS*, 101, 117
- Kraus, A.L., White, R.J., & Hillenbrand, L.A. 2005, *ApJ*, 633, 452
- Ku, W.H.-M., & Chanan, G.A. 1979, *ApJ*, 234, 59
- Leggett, S.K., et al. 2002, *ApJ*, 564, 452
- Leggett, S.K., Allard, F., Berriman, G., Dahn, C.C., & Hauschildt, P.H. 1996, *ApJS*, 104, 117
- Mamajek, E.E. et al. 2004, *ApJ*, 612, 496
- Martín, E.L., Delfosse, X., & Guieu, S. 2004, *AJ*, 127, 449
- Massey, P., Strobel K., Barnes, J.B., & Anderson, E. 1988, *ApJ*, 328, 315
- Meyer, M.R., Calvet, N., & Hillenbrand, L.A. 1997, *AJ*, 114, 288
- Parrao, L., & Schuster, W.J. 2003, *RevMexAA*, 19, 81
- Preibisch, T., Brown, A., Bridges, T., Guenther, E., & Zinnecker, H. 2002, *AJ*, 124 404
- Preibisch et al. 2005, *ApJS*, 160, 401

- Preibisch, T., Guenther, E., & Zinnecker, H. 2001, *AJ*, 121, 1040
- Preibisch, T., Guenther, E., Zinnecker, H., Sterzik, M., Frink, S., & Roeser, S. 1998, *A&A*, 333, 619
- Preibisch, T., & Zinnecker, H. 1999, *AJ*, 117, 2381
- Rabinowitz, D. et al. 2003, *BAAS*, 203, 38.12
- Schlegel, D.J., Finkbeiner, D.P., & Davis, M. 1998, *ApJS*, 500, 525
- Siegler, N., Close, L.M., Cruz, K.L., Martín, E.L., & Reid, I.N. 2005, *ApJ*, 621, 1023
- Silverstone, M.D., et al. 2006, *ApJ*, in press
- Skrutskie, M.F., et al. 1990, *AJ*, 99, 1187
- Slesnick, C.L., Carpenter, J.M., & Hillenbrand, L.A. 2006, in prep
- Slesnick, C.L., Hillenbrand, L.A., & Carpenter, J.M. 2004, *ApJ*, 610, 1045
- Tachibana, S., & Huss, G.R. 2003, *AJ*, 588, 41
- Walter, F.M., Vrba, F.J., Mathieu, R.D., Brown, A., & Myers, P.C. 1994, *AJ*, 107, 692
- White, R.J., & Hillenbrand, L.A. 2004, *ApJ*, 616, 998
- Wiling, B.A., Meyer, M.R., Robinson, J.G., & Greene, T.P. 2005, *astro-ph/0506251*
- de Zeeuw, P.T., Hoogerwerf, R., de Bruijne, J.H.J., Brown, A.G. A., & Blaauw, A. 1999, *AJ*, 177, 354

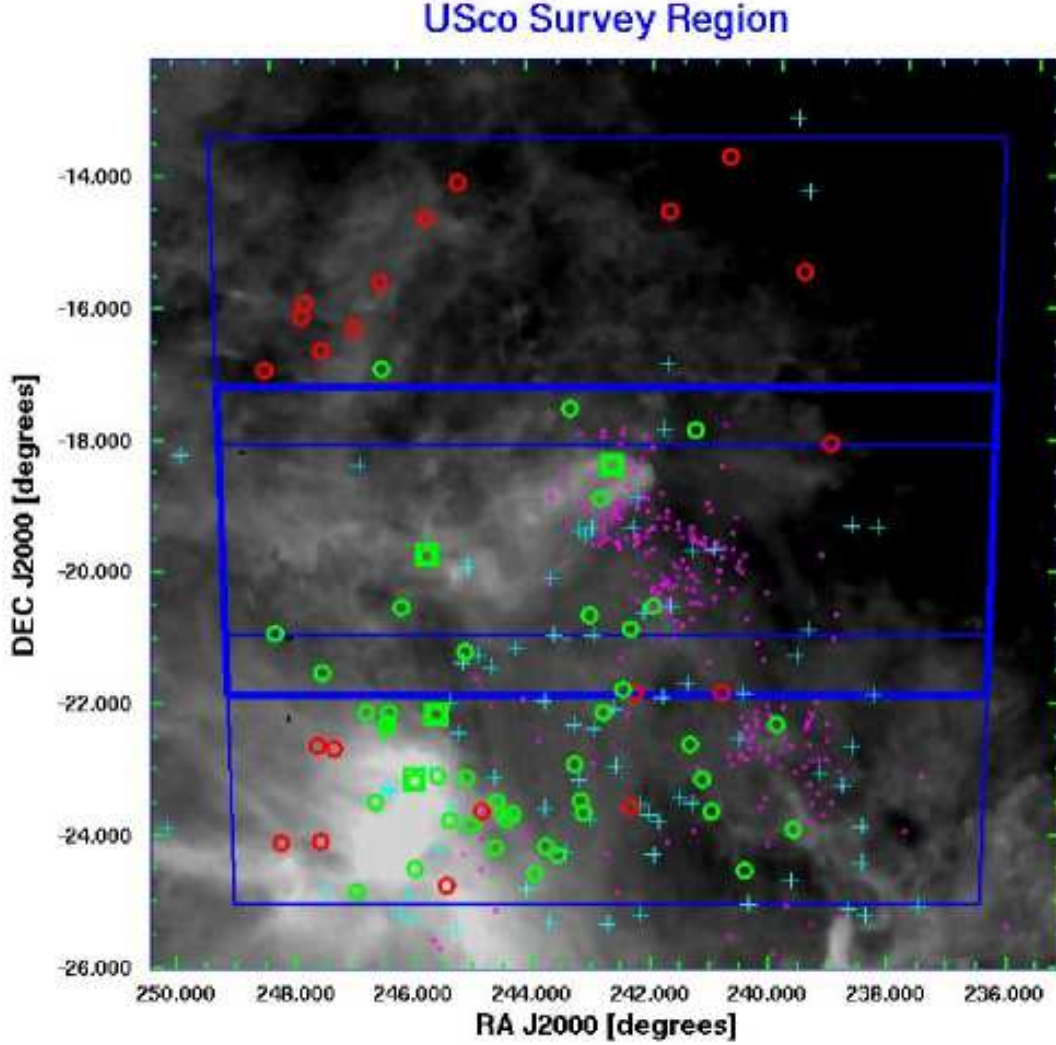


Fig. 1.— Spatial distribution of the USco survey area outlined in blue, overlaid on IRAS 100μm emission. The thicker blue line denotes the outline of the monitoring scan region which was repeated 24 times. New USco members identified from this work (43; green circles) are shown with previously known, spectroscopically confirmed low mass members (196; Sp Type \geq K7 corresponding to $M \leq 0.6 M_{\odot}$ at 5 Myr; small magenta circles) from the literature (see text), high mass Hipparcos members (114; cyan pluses) and spectroscopic targets determined to be field dwarfs (22; red circles). New members which exhibit very strong H α emission are boxed.

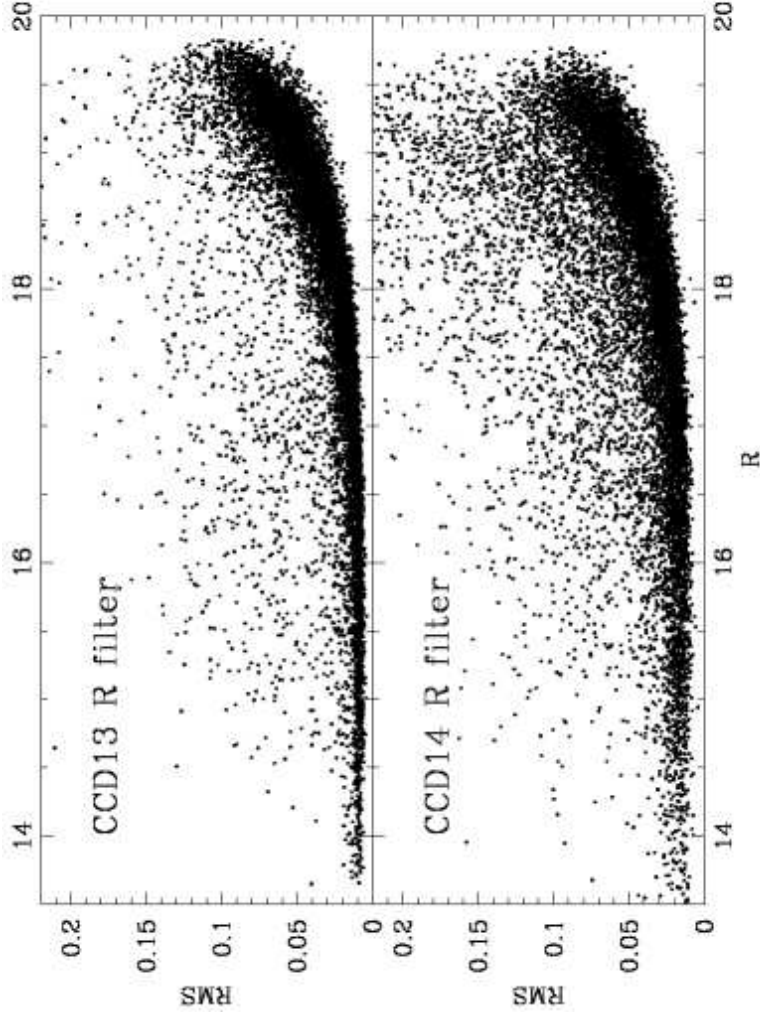


Fig. 2.— Computed RMS deviations as a function of magnitude for two CCDs. Each magnitude is the average of 10–24 measurements and the corresponding RMS is a weighted deviation of all individual measurements about that average. The top and bottom panels show respectively repeatability plots for a ‘best’ and typical CCD. See text for further explanation.

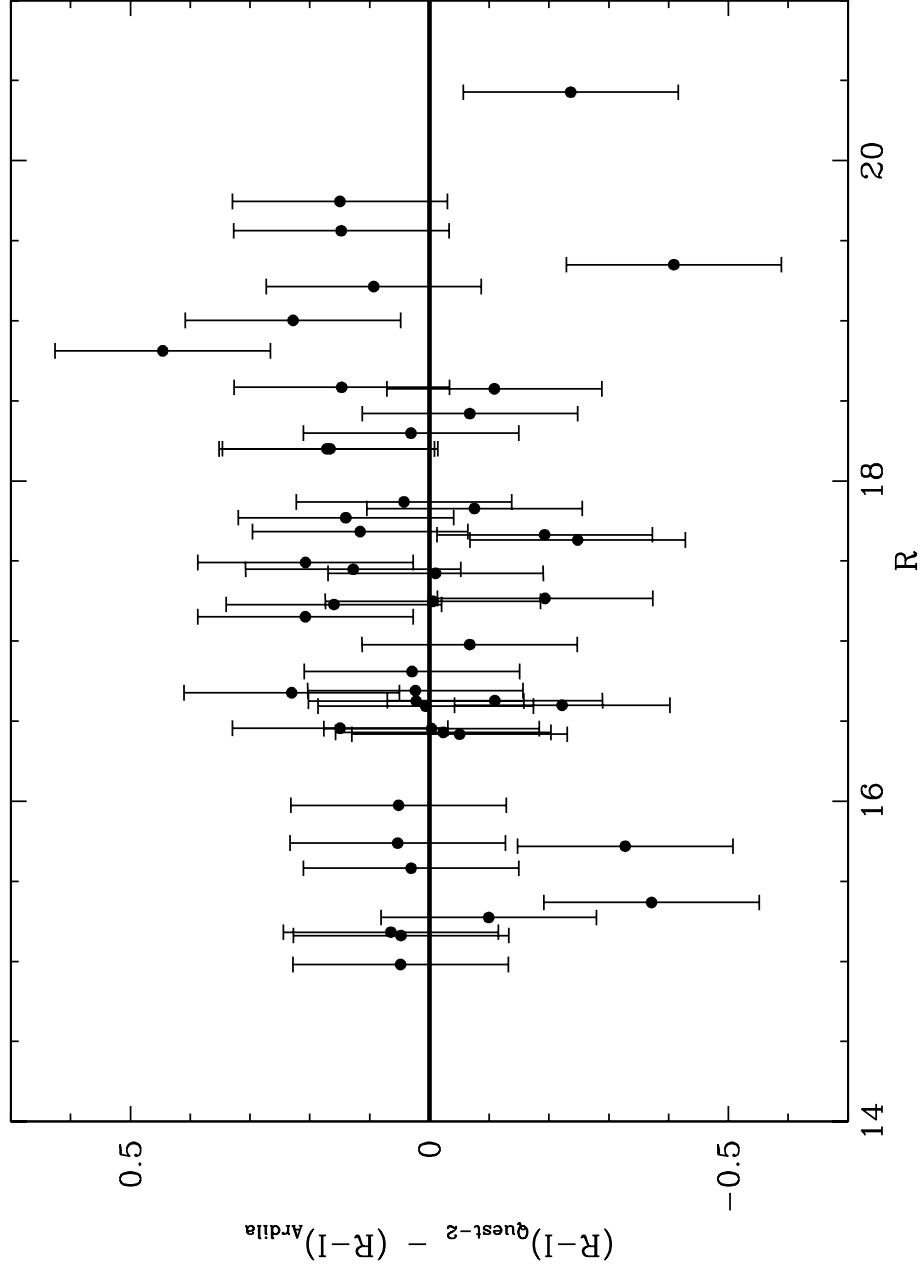


Fig. 3.— Difference between Quest-2 $R-I$ colors and $R-I$ colors from Ardila et al. (2000) (converted to the Johnson system) as a function of Quest-2 R magnitude. Errorbars reflect root-sum squared uncertainties in both datasets.

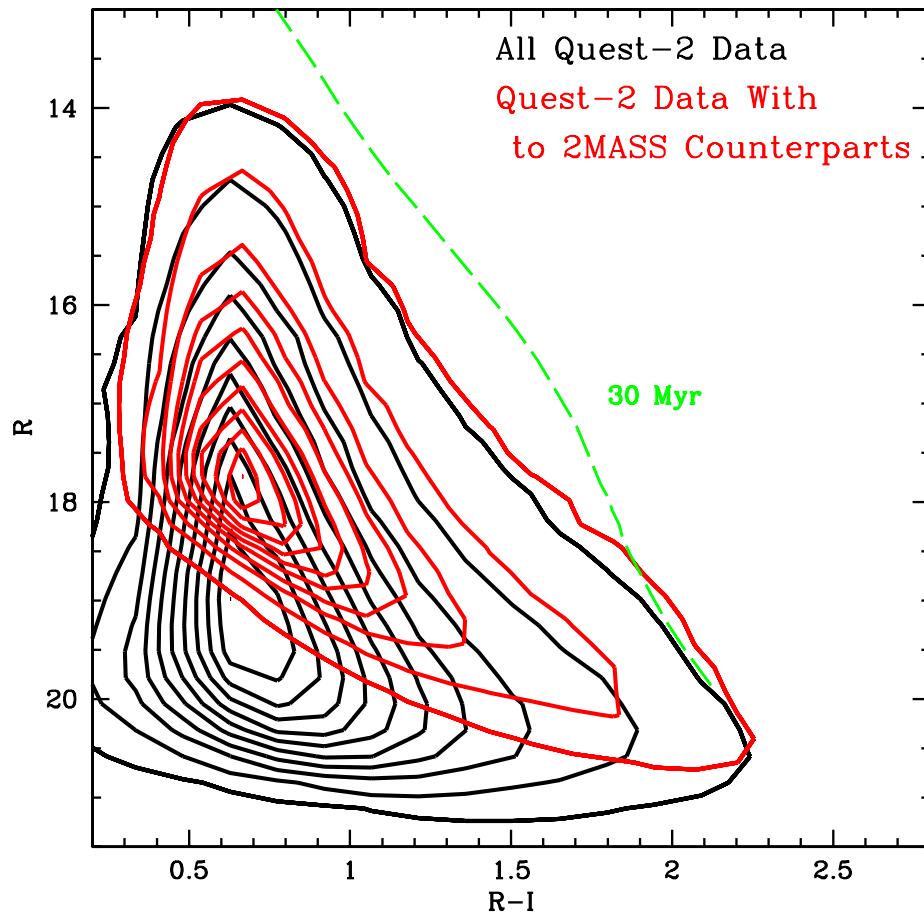


Fig. 4.— Optical color-magnitude diagrams of all Quest-2 sources (black) and those with 2MASS detections (red). For both black and red contours data are represented at 90% to 10% and 3% of the peak level.

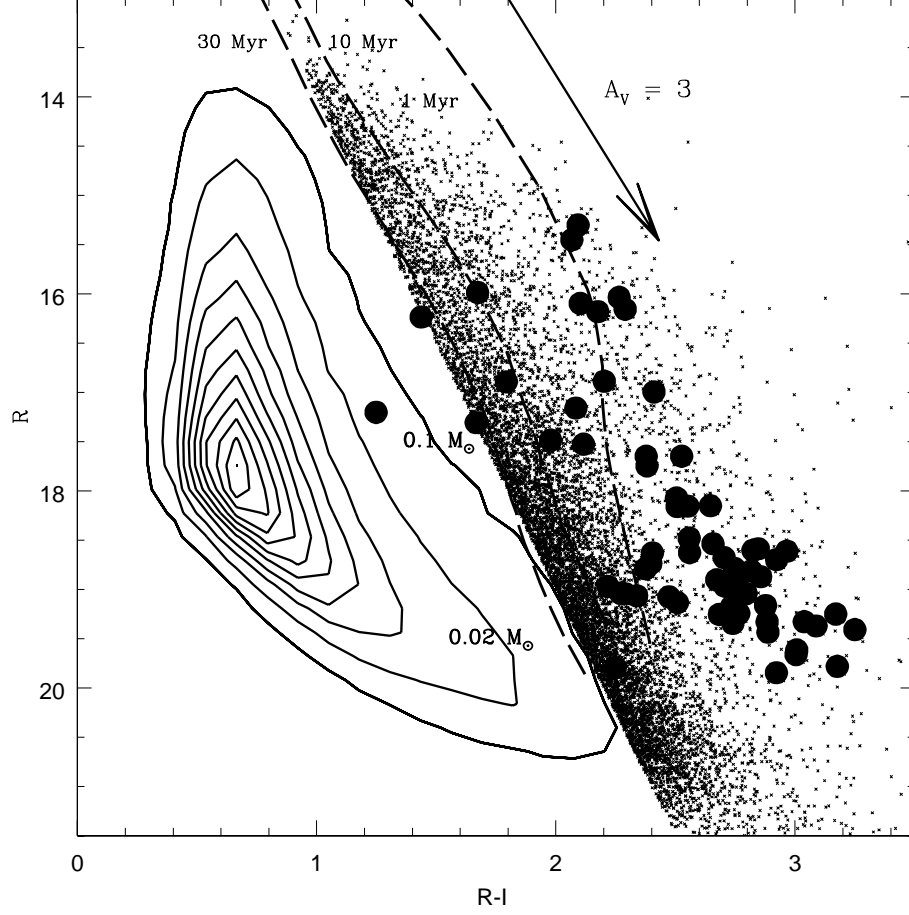


Fig. 5.— $R, R - I$ color-magnitude diagram for all sources with a 2MASS detection, shown with isochrones from DM97 transformed by us into the $R, R - I$ plane. Contours are as described in Figure 4. Objects which appear younger than ~ 30 Myr are shown as discrete points. Spectroscopic targets presented here are shown as large circles.

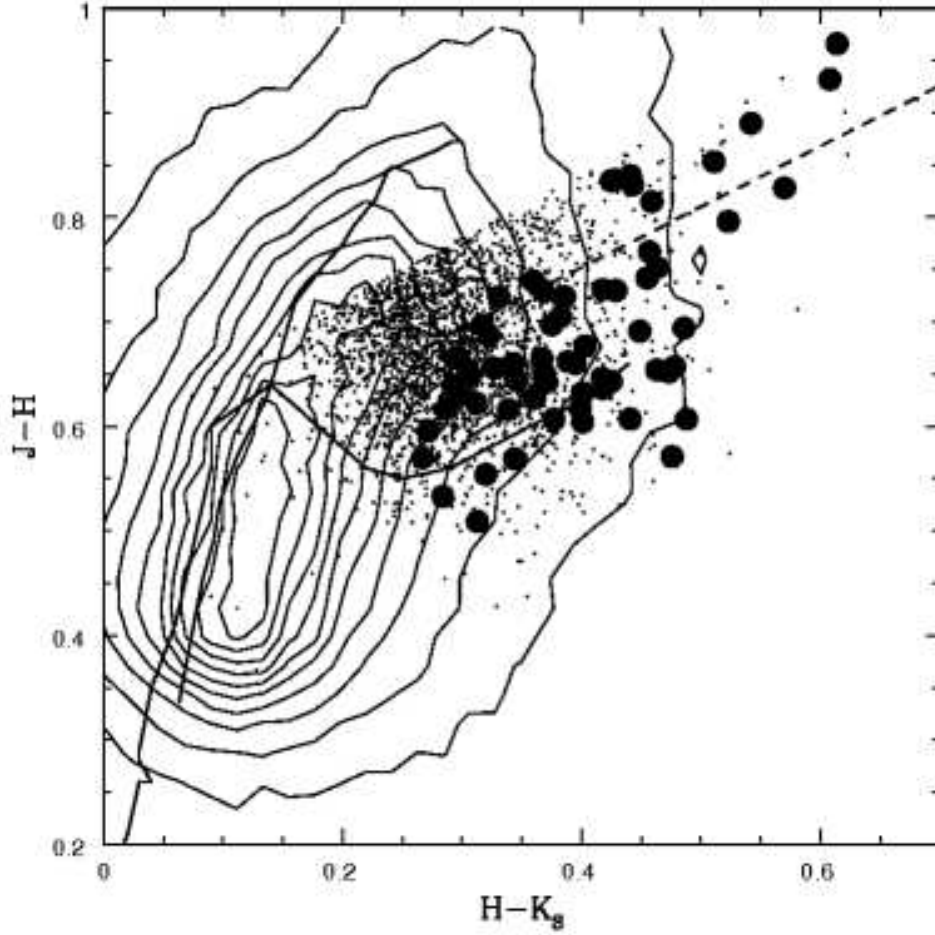


Fig. 6.— 2MASS $J-H$, $H-K_S$ color-color diagram for all data represented as contours at 90% to 10% and 3% of the peak level. Shown as discrete points are all objects which appear younger than 30 Myr in an optical CMD and do not have colors consistent with those of background giants. Solid lines are dwarf zero-age main sequence (O5–M8) and giant loci (G0–M7). The dashed line represents the classical T Tauri locus as defined by Meyer et al. (1997). Spectroscopic targets presented here are shown as large circles.

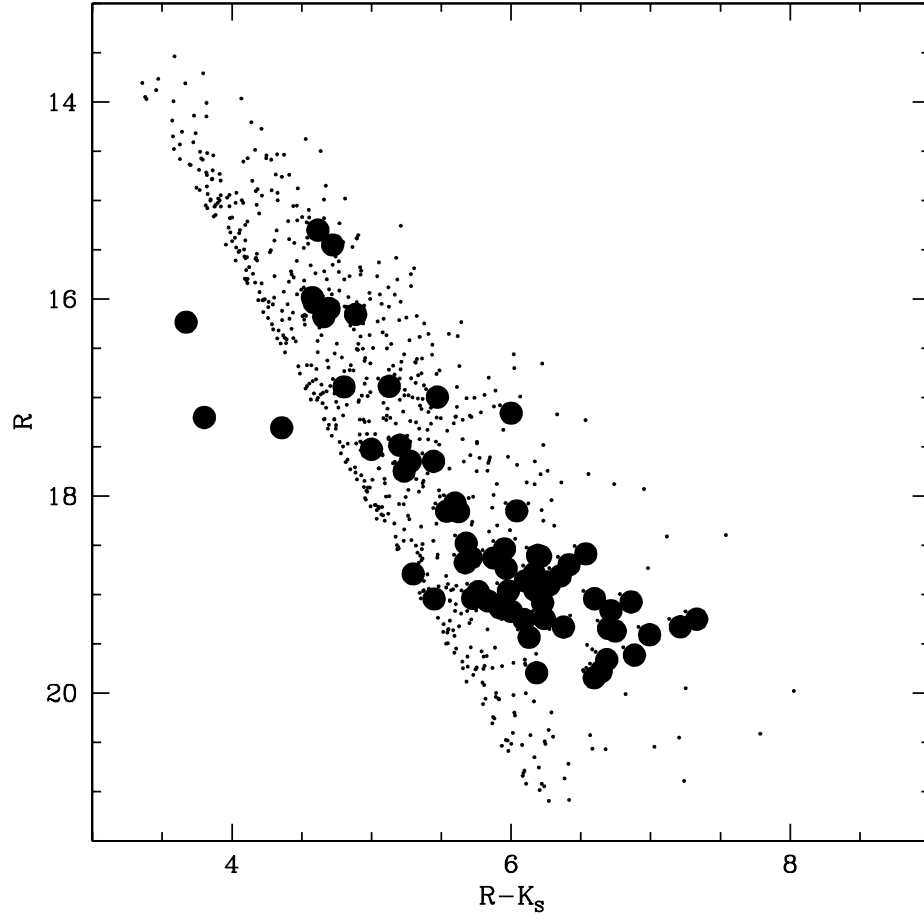


Fig. 7.— $R, R - K$ color-magnitude diagram for the ~ 1000 objects which meet optical and near-infrared selection criteria shown in Figures 5 & 6 and which appear red in $R - K$. Spectroscopic targets presented here are shown as large circles.

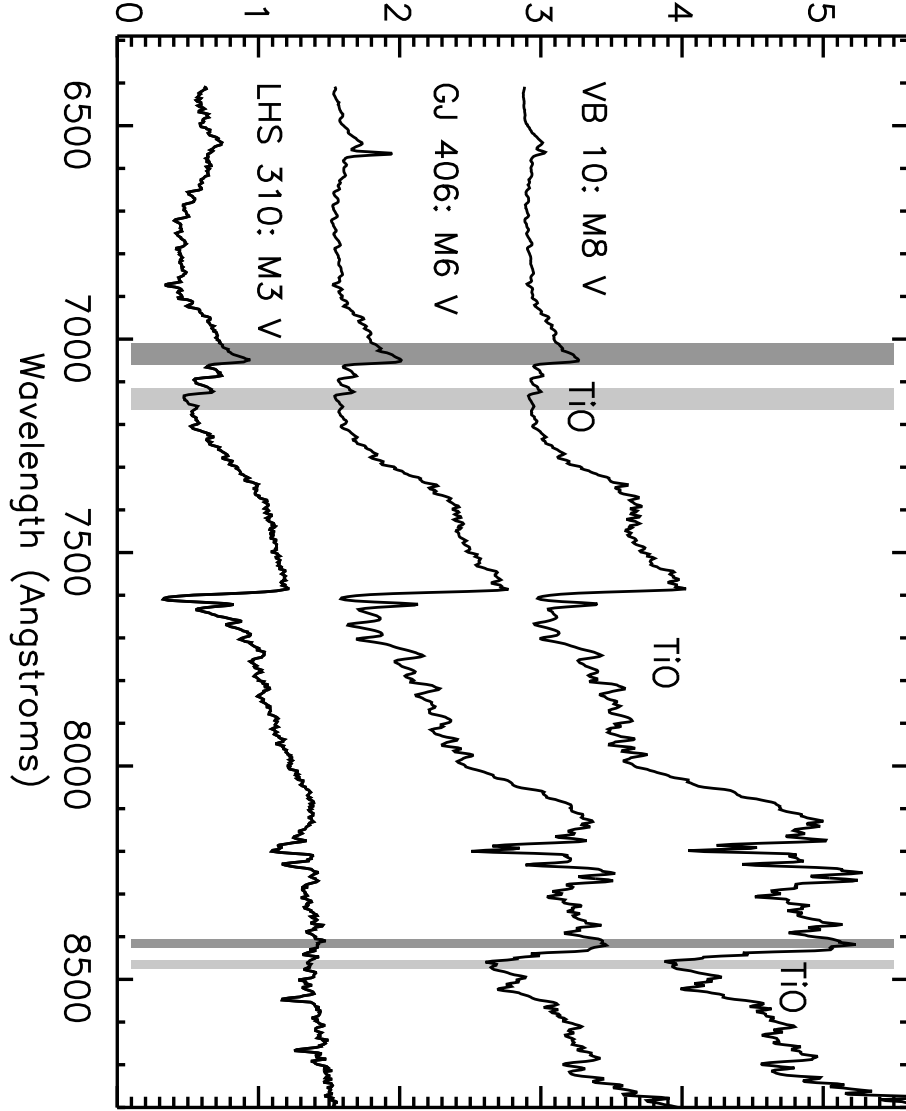


Fig. 8.— Spectra for M3, M6, and M8 type dwarf stars. Dominant TiO features are labeled. Light and dark shaded regions respectively show location of the TiO and continuum bands used in spectral classification.

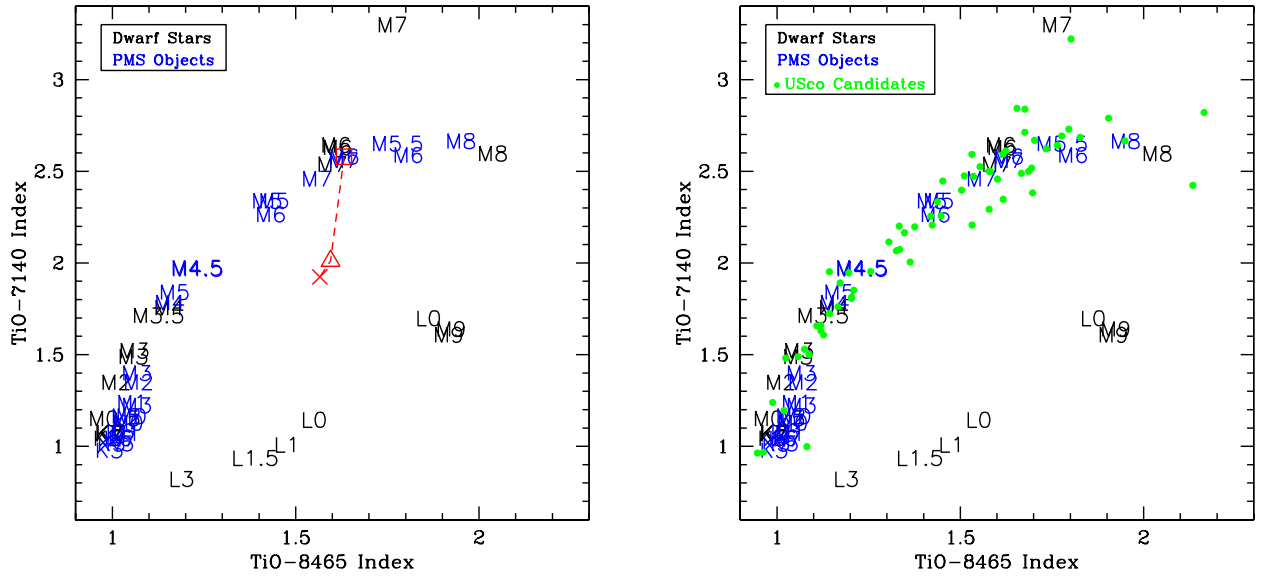


Fig. 9.— Left panel shows two temperature-sensitive indices, TiO-7140 vs TiO-8165. Spectral types represent measured indices for dwarf stars (black) and known USco and Taurus members (blue). The right panel adds green circles corresponding to measured indices for program stars. In the left panel, connected red symbols indicate the effects of veiling from a cool circumstellar disk (box) or a hot accretion shock (triangle and ‘X’) on measured indices for a single star (see text for more details).

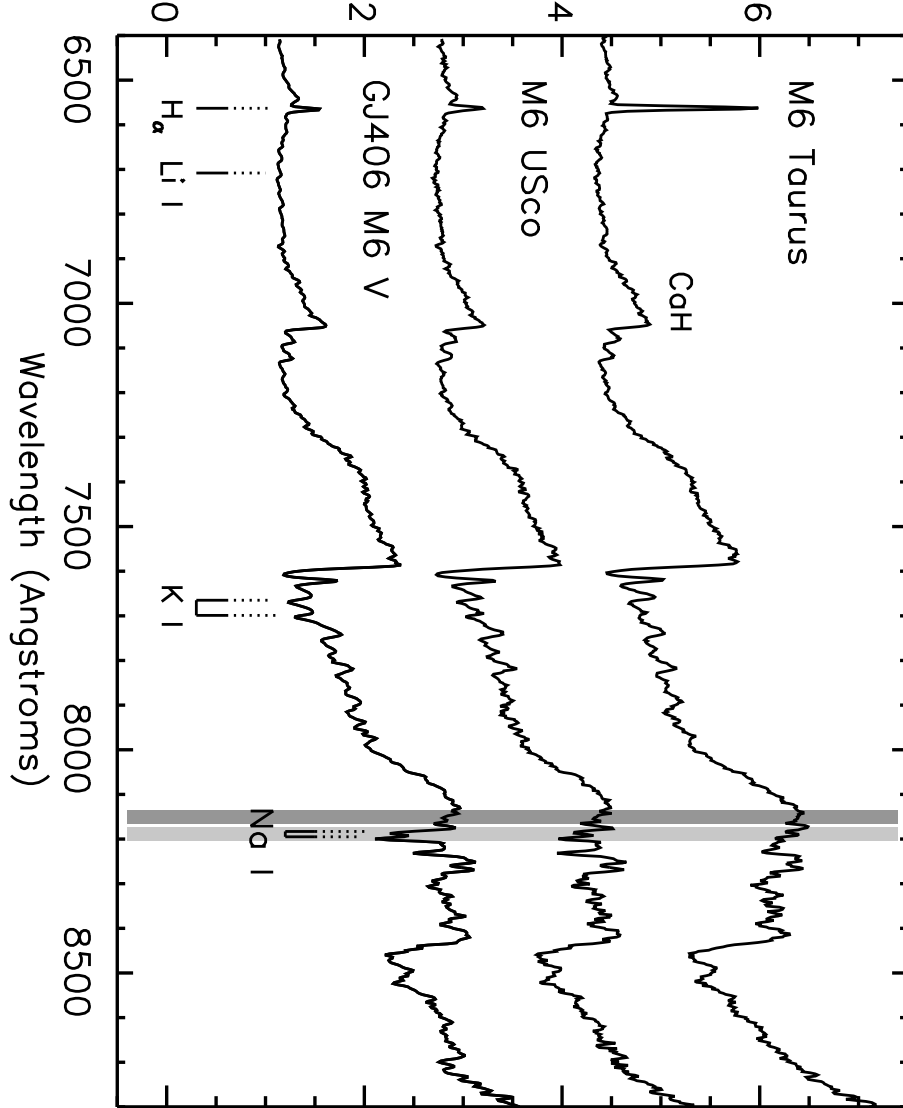


Fig. 10.— Sequence of three M6 stars: a high-gravity main-sequence star (GJ406), a 5-Myr intermediate-gravity USco object (DENIS-P16007.5-181056.4) and a 1-Myr Taurus object (MH05). Gravity- sensitive absorption features are labeled and increase with increasing stellar age and gravity. Light and dark shaded regions respectively show location of the Na and continuum bands used in surface gravity analysis.

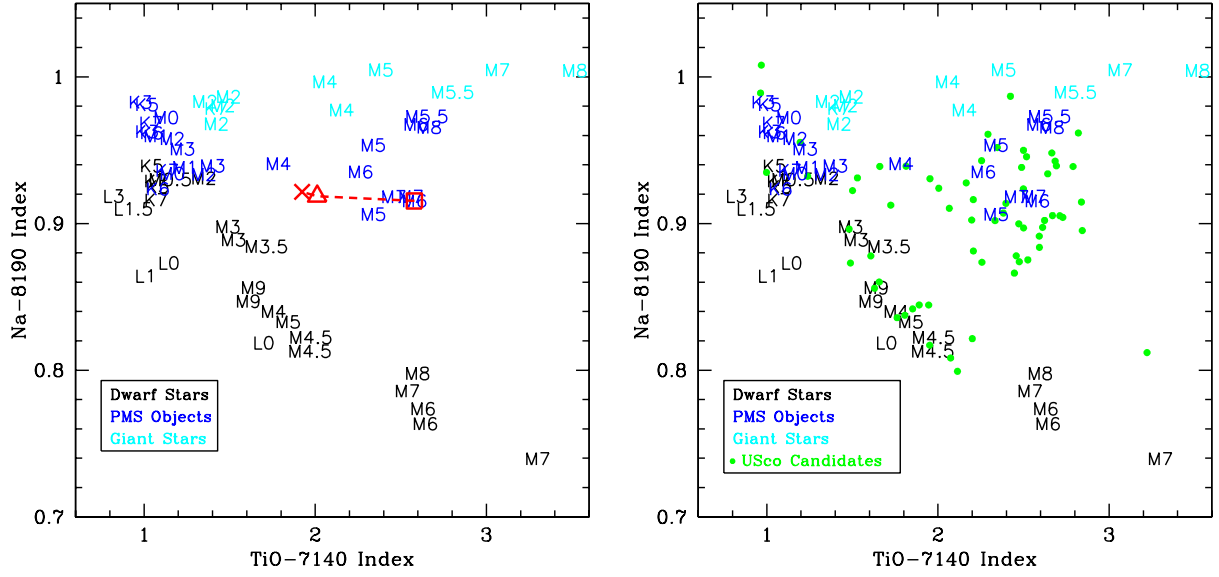


Fig. 11.— Same as Figure 9 but for the TiO-7140 index vs. the gravity-sensitive Na-8195 index. Cyan spectral types represent measured indices for low gravity giant stars.

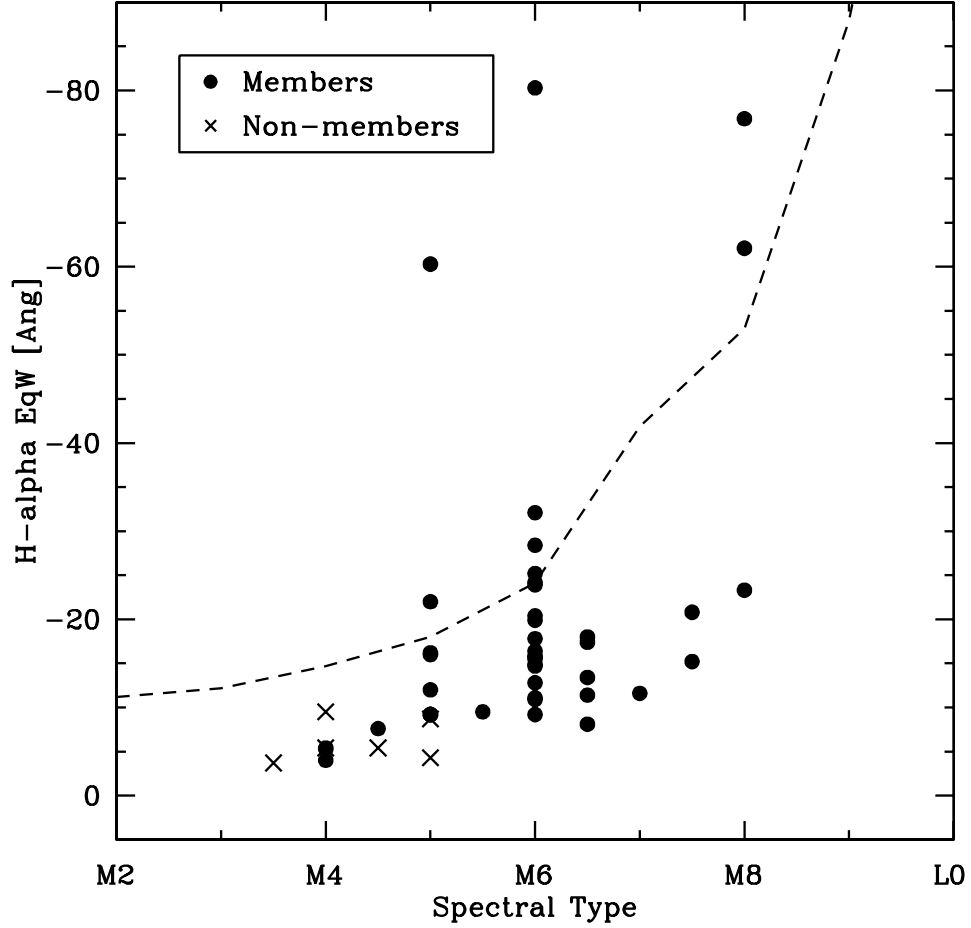


Fig. 12.— Measured $H\alpha$ equivalent widths for all spectra with measurable $H\alpha$ as a function of spectral type. Circles represent objects confirmed to be new members; 'X's represent objects confirmed to be field dwarfs. The dotted line is the empirical accretor/non-accretor upper limit derived by Barrados y Navascués & Martín (2003).

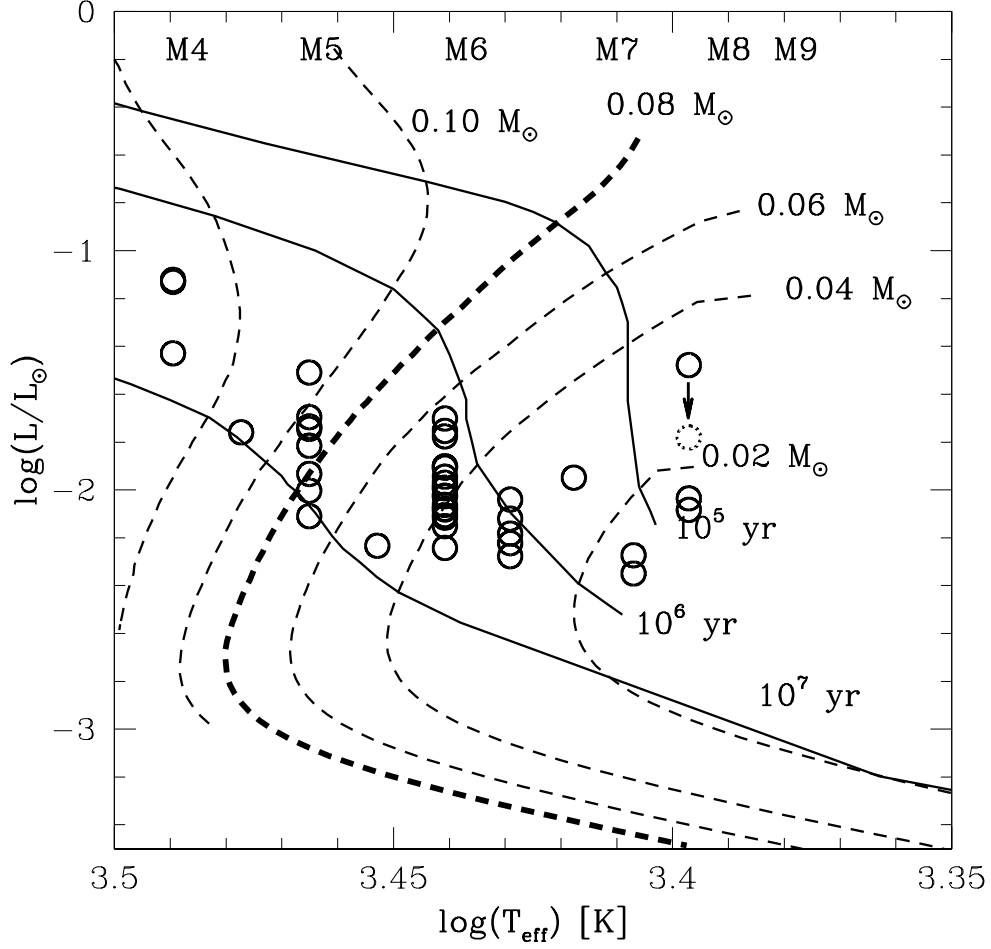


Fig. 13.— HR diagram for new PMS objects found in this work, shown with model tracks and isochrones of DM97. The sample is consistent with an age of ~ 5 Myr and contains masses spanning the brown dwarf to stellar regimes.

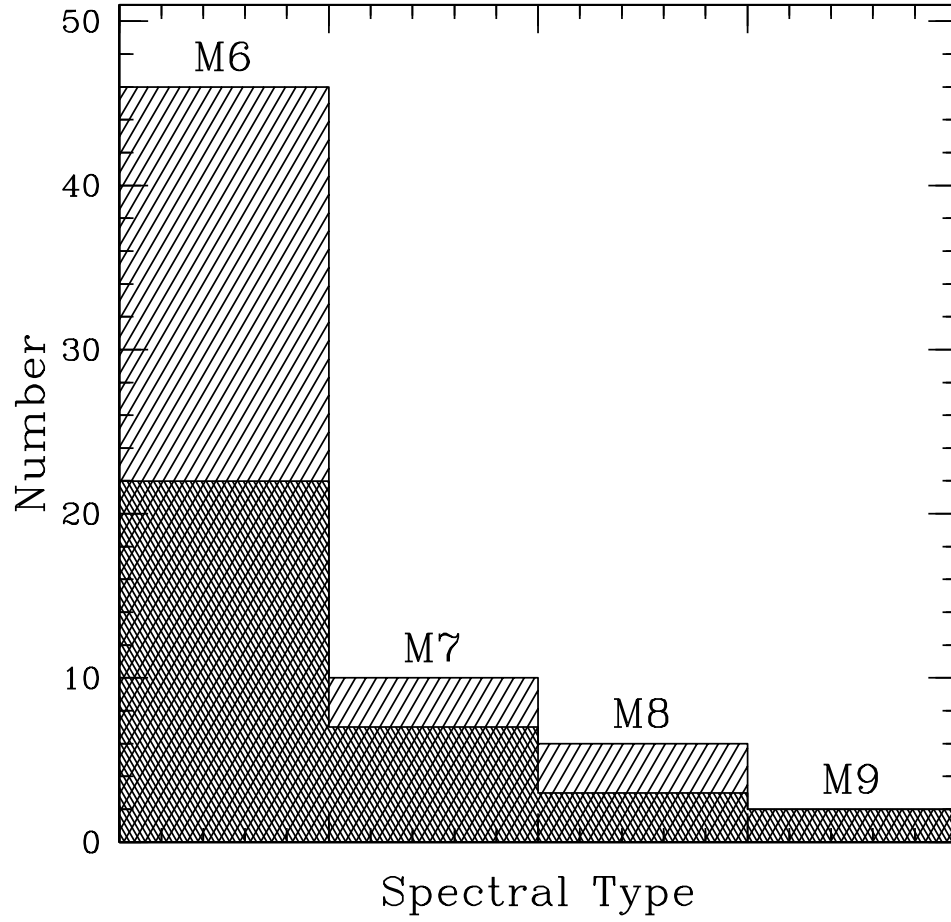


Fig. 14.— Histogram of the number of brown dwarfs spectroscopically confirmed in USco with the addition of our work (light shading) compared to a compilation of all previous results (dark shading).

Table 1. Measured Quantities for PMS Candidates with Observed Spectra

ID	R	I	J ^c	H ^c	K _S ^c	TiO-7140	TiO-8165	Na-8195	SpType ^d	$W(H\alpha)$ [Å]	Gravity ^e
SCH15563309-18074323	19.7	16.5	14.18	13.61	13.13	3.22	1.80	0.81	M7	–	dwarf
SCH15582384-15310335	16.1	13.9	12.36	11.79	11.52	1.76	1.16	0.83	M4.5	-5.40	dwarf
SCH15583162-24025411	17.5	15.0	13.16	12.51	12.20	1.95	1.25	0.93	M4.5	-7.60	USco
SCH15594802-22271650	19.1	16.5	14.24	13.56	13.16	2.78	1.90	0.93	M7.5	-15.20	USco
SCH16014768-24410152	18.5	15.9	13.87	13.27	13.00	2.44	1.45	0.86	M5	-16.00	USco
SCH16031129-13454481	17.2	15.5	13.96	13.35	12.95	2.07	1.33	0.80	M5	-8.70	dwarf
SCH16032871-21583609 ^a	18.9	16.7	14.62	13.96	13.59	0.99	1.08	0.93	K3:	–	dwarf
SCH16040453-23463795	15.3	13.3	11.74	11.04	10.73	1.81	1.20	0.93	M4	-4.00	int
SCH16044303-23182620 ^b	19.0	15.9	13.81	13.19	12.85	2.72	1.79	0.90	M6.5	-18.00	USco
SCH16051829-17562092	15.2	13.1	11.64	10.98	10.68	1.66	1.11	0.93	M4	-5.40	int
SCH16053077-22462016	18.8	16.1	13.78	13.18	12.78	2.84	1.65	0.89	M6	-17.80	USco
SCH16070403-14352587	15.9	14.2	12.28	11.73	11.41	1.89	1.17	0.84	M4	–	dwarf
SCH16075850-20394890	18.4	15.8	13.59	12.95	12.58	2.47	1.53	0.89	M6	-14.90	USco
SCH16091254-21582262	18.7	16.3	14.39	13.77	13.49	2.20	1.33	0.82	M5	–	dwarf
SCH16092940-23431209	19.0	16.5	14.20	13.57	13.21	0.96	0.96	1.00	<K3:	–	dwarf
SCH16093018-20595409	18.8	16.2	13.99	13.35	12.98	2.59	1.53	0.89	M6	-11.10	USco
SCH16095991-21554293	19.3	16.4	14.30	13.64	13.30	2.49	1.57	0.89	M6.5	-17.40	USco
SCH16103876-18292353	19.2	16.5	13.96	13.16	12.64	2.29	1.57	0.96	M6	-80.30	USco
SCH16111711-22171749	19.7	16.8	14.34	13.73	13.25	2.68	1.82	0.94	M7.5	-20.80	USco
SCH16112959-19002921	19.0	16.2	13.67	12.90	12.44	2.49	1.68	0.94	M6	-20.40	USco
SCH16121188-20472698	18.7	15.9	13.66	13.02	12.60	2.69	1.77	0.93	M6.5	-8.10	USco
SCH16123758-23492340	18.5	16.0	13.93	13.28	12.91	2.47	1.51	0.87	M6	-15.80	USco
SCH16124692-23384086	18.7	15.9	13.65	13.02	12.62	2.66	1.70	0.90	M6	-14.70	USco
SCH16131212-23050329	19.1	16.4	14.05	13.44	13.00	2.62	1.73	0.90	M6.5	-13.40	USco
SCH16132576-17373542	16.0	13.9	12.32	11.69	11.40	1.72	1.14	0.91	M4	-5.30	int
SCH16141974-24284053	18.7	16.0	13.81	13.15	12.76	2.59	1.61	0.88	M6	-16.40	USco
SCH16151115-24201556	19.0	16.3	14.23	13.58	13.17	2.33	1.43	0.90	M6	-10.90	USco
SCH16155508-24443677	18.6	15.7	13.39	12.74	12.28	2.48	1.66	0.93	M6	-15.80	USco
SCH16172504-23503799	18.8	16.1	13.74	13.01	12.63	2.25	1.44	0.87	M5	-12.00	USco
SCH16174540-23533618	19.2	16.3	14.05	13.31	12.95	2.83	1.67	0.91	M6	-15.50	USco
SCH16182501-23381068	18.9	16.1	13.72	12.88	12.44	2.06	1.32	0.91	M5	-9.20	USco
SCH16183144-24195229	19.5	16.6	14.15	13.46	12.97	2.45	1.60	0.87	M6.5	-11.40	int
SCH16192530-23470717	18.5	16.1	14.01	13.17	12.75	1.60	1.12	0.87	M4	–	dwarf
SCH16200756-23591522	18.5	15.6	13.21	12.48	12.05	2.49	1.58	0.92	M6	-24.20	USco
SCH16202127-21202923	18.5	15.5	13.39	12.74	12.40	2.61	1.62	0.89	M6	-23.90	USco
SCH16202523-23160347	18.9	16.6	14.37	13.68	13.23	2.20	1.53	0.88	M5.5	-9.50	USco
SCH16202753-14082840	16.0	13.8	12.22	11.56	11.27	1.85	1.20	0.84	M4.5	–	dwarf
SCH16213591-23550341	19.5	16.5	13.94	13.19	12.73	2.38	1.69	0.90	M6	-19.90	USco
SCH16214806-24542504	19.7	17.4	15.19	14.22	13.61	1.23	0.98	0.93	M2	–	dwarf
SCH16221577-23134936	18.3	15.8	13.71	13.14	12.80	2.52	1.55	0.87	M6	-9.20	int
SCH16222156-22173094	18.0	15.5	13.74	13.09	12.61	2.00	1.36	0.92	M5	-60.30	USco
SCH16223315-14422746	17.6	15.3	13.49	12.84	12.51	2.11	1.30	0.79	M5	–	dwarf
SCH16224384-19510575	17.0	15.0	12.35	11.61	11.15	2.42	2.13	0.98	M8	-62.10	USco
SCH16235158-23172740	19.3	16.1	13.55	12.89	12.41	2.82	2.16	0.96	M8	-76.80	USco
SCH16235474-24383211	19.1	16.0	13.31	12.49	11.92	2.34	1.61	0.95	M6	-12.80	USco
SCH16242880-20385513	18.9	16.7	14.58	13.77	13.31	1.50	1.08	0.92	M3	–	dwarf

Table 1—Continued

ID	R	I	J ^c	H ^c	K _S ^c	TiO-7140	TiO-8165	Na-8195	SpType ^d	$W(H\alpha)$ [Å]	Gravity ^e
SCH16252609-15401969	17.4	15.3	13.67	12.94	12.52	1.52	1.07	0.93	M3	–	dwarf
SCH16252862-16585055	19.2	16.2	13.67	13.01	12.62	2.66	1.94	0.94	M8	-23.30	USco
SCH16252968-22145448	18.0	15.4	13.19	12.49	12.11	2.25	1.41	0.94	M5	-16.20	USco
SCH16253671-22242887	18.7	15.9	13.53	12.83	12.45	2.64	1.76	0.93	M7	-11.60	USco
SCH16254319-22300300	16.8	15.0	13.02	12.40	12.09	2.19	1.37	0.90	M5	-9.20	USco
SCH16263026-23365552	18.9	16.5	13.75	12.82	12.21	2.51	1.69	0.94	M6	-32.10	USco
SCH16265619-22135224	18.5	15.7	13.48	12.83	12.41	2.71	1.67	0.90	M6	-28.40	USco
SCH16270959-16204810	17.4	15.4	13.55	12.72	12.28	1.19	1.01	0.95	M2	–	dwarf
SCH16274801-24571371	19.2	16.2	13.54	12.65	12.11	2.20	1.42	0.91	M5	-22.00	USco
SCH16290665-22464968	18.6	16.2	14.03	13.19	12.77	1.65	1.10	0.86	M4	-9.50	dwarf
SCH16291911-16410107	16.8	14.6	12.85	12.12	11.76	1.62	1.11	0.85	M3.5	-3.70	dwarf
SCH16294877-21370914	16.9	14.5	12.52	11.86	11.52	2.16	1.34	0.92	M5	-9.20	USco
SCH16300911-24111718 ^a	16.1	14.7	13.38	12.84	12.56	1.48	1.05	0.87	M2	–	dwarf
SCH16301483-22435159	18.8	16.7	14.57	13.71	13.20	1.48	1.02	0.89	M3	–	dwarf
SCH16301682-15574807	18.0	15.6	13.59	12.86	12.53	1.95	1.14	0.81	M5	-4.30	dwarf
SCH16303166-16093250	17.5	15.2	13.38	12.69	12.37	1.80	1.20	0.83	M4	-5.40	dwarf
SCH16324726-20593771	17.9	15.5	13.45	12.85	12.47	2.39	1.50	0.91	M6	-25.20	USco
SCH16325276-24110013 ^a	17.1	15.9	14.33	13.69	13.40	0.96	0.94	0.98	<K3	–	dwarf
SCH16325602-16582835	15.9	13.7	12.26	11.76	11.44	1.94	1.19	0.84	M4	–	dwarf

^aPhotometry for three targets changed significantly after spectroscopic observations took place, such that they would no longer have been chosen as photometric candidates.

^bThe only object among our spectral targets previously identified in the literature is SCH16044303-23182620 corresponding to UScoC-TIO110 (Ardila et al. 2000).

^cNear-infrared photometry taken from 2MASS.

^dSpectral type errors are ± 0.5 for M subclasses. A ‘:’ indicates a spectral type is less certain.

^eQualitative surface gravity type ‘USco’ and ‘dwarf’ labels indicate a star has surface gravity signatures consistent with those measured for known USco members or field dwarfs. A value of ‘int’ corresponds to the object having gravity signatures between those of known USco members and field dwarfs.

Table 2. Derived Quantities for New USco Members

ID	M_J	A_V	$\log(T_{eff}/K)$	$\text{Log } (L/L_\odot)$
SCH15583162-24025411	7.18	0.66	3.48	-1.76
SCH15594802-22271650	8.35	0.33	3.41	-2.27
SCH16014768-24410152	8.03	0.15	3.47	-2.11
SCH16040453-23463795	5.64	1.14	3.49	-1.13
SCH16044303-23182620	7.99	0.05	3.43	-2.12
SCH16051829-17562092	5.62	0.85	3.49	-1.12
SCH16053077-22462016	7.97	0.04	3.44	-2.11
SCH16075850-20394890	7.69	0.38	3.44	-1.99
SCH1609301820595409	8.09	0.39	3.44	-2.15
SCH16095991-21554293	8.38	0.43	3.43	-2.28
SCH16103876-18292353	7.69	1.78	3.44	-1.99
SCH16111711-22171749	8.54	0.00	3.41	-2.35
SCH16112959-19002921	7.46	1.52	3.44	-1.90
SCH16121188-20472698	7.79	0.24	3.43	-2.04
SCH16123758-23492340	8.00	0.48	3.44	-2.12
SCH16124692-23384086	7.77	0.29	3.44	-2.02
SCH16131212-23050329	8.25	0.00	3.43	-2.22
SCH16132576-17373542	6.38	0.52	3.49	-1.43
SCH16141974-24284053	7.87	0.54	3.44	-2.06
SCH16151115-24201556	8.32	0.42	3.44	-2.24
SCH16155508-24443677	7.46	0.49	3.44	-1.90
SCH16172504-23503799	7.59	1.31	3.47	-1.93
SCH16174540-23533618	7.91	1.26	3.44	-2.08
SCH16182501-23381068	7.29	2.37	3.47	-1.82
SCH16183144-24195229	8.15	0.76	3.43	-2.18
SCH16200756-23591522	7.09	1.18	3.44	-1.75
SCH16202127-21202923	7.48	0.41	3.44	-1.91
SCH16202523-23160347	8.31	0.95	3.45	-2.23
SCH16213591-23550341	7.78	1.38	3.44	-2.03
SCH16221577-23134936	7.91	0.00	3.44	-2.08
SCH16222156-22173094	7.76	0.66	3.47	-2.00

Table 2—Continued

ID	M_J	A_V	$\log(T_{eff}/K)$	$\text{Log } (L/L_\odot)$
SCH16224384-19510575	6.35	0.75	3.40	-1.48
SCH16235158-23172740	7.75	0.00	3.40	-2.04
SCH16235474-24383211	6.96	2.07	3.44	-1.70
SCH16252862-16585055	7.86	0.02	3.40	-2.08
SCH16252968-22145448	7.09	1.14	3.47	-1.73
SCH16253671-22242887	7.55	0.67	3.42	-1.95
SCH16254319-22300300	7.12	0.38	3.47	-1.74
SCH16263026-23365552	7.15	3.02	3.44	-1.78
SCH16265619-22135224	7.57	0.39	3.44	-1.94
SCH16274801-24571371	6.99	2.82	3.47	-1.70
SCH16294877-21370914	6.53	0.73	3.47	-1.51
SCH16324726-20593771	7.64	0.06	3.44	-1.97